

Spitzer Transit and Secondary Eclipse Photometry of GJ 436b

Drake Deming

Planetary Systems Laboratory

Goddard Space Flight Center, Code 693, Greenbelt MD 20771

Joseph Harrington

Department of Physics,

Univ. of Central Florida, Orlando, FL 32816

Gregory Laughlin

Department of Astronomy and Astrophysics,

Univ. of California at Santa Cruz, Santa Cruz CA 95064

Sara Seager

Department of Physics, and Department of Earth, Atmosphere and Planetary Sciences,

Massachusetts Institute of Technology, Cambridge MA 02159

Sarah B. Navarro & William C. Bowman

Department of Physics,

Univ. of Central Florida, Orlando, FL 32816

and

Karen Horning

Department of Physics & Space Sciences,

Florida Inst. of Technology, Melbourne FL 32901

Submitted to ApJ Letters

ABSTRACT

We report the results of infrared ($8\mu\text{m}$) transit and secondary eclipse photometry of the hot Neptune exoplanet, GJ 436b using *Spitzer*. The nearly photon-limited precision of these data allow us to measure an improved radius for the planet, and to detect the secondary eclipse. The transit (centered at $HJD = 2454280.78149 \pm 0.00016$) shows the flat-bottomed shape typical of infrared transits, and it precisely defines the planet-to-star radius ratio (0.0839 ± 0.0005), independent of the stellar properties. However, we obtain the planetary radius, as well as the stellar mass and radius, by fitting to the transit curve simultaneously with an empirical mass-radius relation for M-dwarfs ($M = R$). We find $R_* = M_* = 0.47 \pm 0.02$ in solar units, and $R_p = 27,600 \pm 1170$ km (4.33 ± 0.18 Earth radii). This radius significantly exceeds the radius of a naked ocean planet, and requires a gaseous hydrogen-helium envelope. The secondary eclipse occurs at phase 0.587 ± 0.005 , proving a significant orbital eccentricity ($e = 0.150 \pm 0.012$). The amplitude of the eclipse ($5.7 \pm 0.8 \times 10^{-4}$) indicates a brightness temperature for the planet of $T = 712 \pm 36\text{K}$. If this is indicative of the planet’s physical temperature, it suggests the occurrence of tidal heating in the planet. An uncharacterized second planet likely provides ongoing gravitational perturbations that maintain GJ 436b’s orbit eccentricity over long time scales.

Subject headings: Planetary systems - stars: individual (GJ 436) - stars: low mass - stars: fundamental parameters - infrared: stars - eclipses

1. Introduction

The transit and secondary eclipse of an extrasolar planet allow us to deduce its physical properties to a degree that is not possible in other observing geometries (Charbonneau et al. 2007). GJ 436b (Butler et al. 2004) was recently discovered to be the first transiting Neptune-sized planet (Gillon et al. 2007a), opening new parameter space for exoplanet studies. It orbits an M-dwarf star lying 10 pc from our solar system (Maness et al. 2007). In order to constrain the bulk composition and internal structure of transiting planets (Seager et al. 2007; Fortney et al. 2007), precise radii and temperature measurements are needed. The relatively small size of GJ 436A (~ 0.4 solar radii) enhances the planet-to-star contrast during transit and eclipse. Nevertheless, the shallow depth of the GJ 436b transit (0.006) is a challenge for ground-based photometry. Although ground-based observers are achieving impressive levels of precision (Winn et al. 2007), photometry from space-borne platforms remains the preferred observational technique for the highest-precision transit measurements. This is especially true for secondary eclipse, where *Spitzer* measurements have been dominant (Charbonneau et al. 2005; Deming et al. 2005, 2006; Harrington et al. 2007; Knutson et al. 2007).

In this Letter, we report *Spitzer* 8 μm transit and eclipse observations of GJ 436b, and we use these data to refine estimates of the planet’s radius, temperature, and internal structure.

2. Observations

The announcement of GJ 436b transits (Gillon et al. 2007a) was fortuitously concurrent with a window of observability using *Spitzer*. Accordingly, we immediately scheduled observations of one transit, and one secondary eclipse, under our GO-3 Target of

Opportunity (ToO) Program (J. Harrington, P.I.). Since the precision required for measurements of this type is daunting, observations must be carefully designed to limit instrumental systematics (Harrington et al. 2007). Moreover, the reported eccentricity of the GJ 436b orbit (Maness et al. 2007) adds significant uncertainty to the timing of the secondary eclipse observations. Our community ToO program thus works with cooperating teams to design observations and analyze data in line with the best practices gleaned from experience. We solicit collaborations from cooperating teams that discover suitable targets.

Both observational sequences for GJ 436 used the IRAC instrument (Fazio et al. 2004) in subarray mode, at $8\ \mu\text{m}$ only. The transit sequence consisted of 0.4-second exposures in blocks of 64, obtaining 445 blocks (204 minutes). The secondary eclipse sequence was the same, but used 780 blocks (356 minutes). We planned the eclipse observations based on 10^4 bootstrap trial fits to the Doppler data (Maness et al. 2007), to define the probability distribution of eclipse time. Because of the well known ramp-up in the sensitivity of the IRAC $8\ \mu\text{m}$ detector during long observing sequences (Knutson et al. 2007; Harrington et al. 2007), we offset the transit observations to begin ~ 2 hours before transit center.

3. Data Analysis

3.1. Photometry

Because GJ 436 is bright at $8\ \mu\text{m}$, and the zodiacal background is weak in comparison, simple aperture photometry attains nearly photon-limited precision. Our photometry first applies the calibration information contained in the FITS headers, to convert the signal levels to electrons. Within each 64-frame block, we drop the first frame and the 58th frame, due to known instrumental effects (Harrington et al. 2007; Knutson et al. 2007). We examine the time variation of signal level for each pixel in the remaining 62 frames, and

correct pixels in frames that are discrepant by $> 4\sigma$ to the median value for that pixel (this removes energetic particle hits). We sum the intensity in an 8- by 8-pixel square aperture centered on the star in each frame, including fractional pixels, and sum again over the 62 frames in the block. We varied the aperture size to verify that an 8-pixel box produced the lowest noise, but this dependence is not strong. We fit a Gaussian to the peak in a histogram of pixel intensities for each block to determine, and subtract, the average background level. We used the same background value for all 62 frames in a block.

We calculated the expected noise level for the photometry, based on the Poisson electron counting noise (dominant), and read noise (small). Comparing the aperture photometry for the 62 frames within each block, we find that these photometry errors are distributed as Gaussian noise, with a dispersion merely 3.5% greater than predicted. The intensities for the 445 transit blocks are illustrated in Figure 1, top panel. We examined the block-to-block variation in intensity for these points after removing the best transit fit, and we find a Gaussian distribution, with a standard deviation of 7×10^{-4} . Since we detect $\sim 3.1 \times 10^6$ electrons per block (Figure 1), we expect a photon-limited precision of 5.7×10^{-4} . We thus attain about 80% of photon-limited S/N, consistent with previous *Spitzer* photometry at this wavelength (Knutson et al. 2007; Harrington et al. 2007).

IRAC photometry at 8 μm is known to exhibit a gradually increasing ramp-up in sensitivity, due to filling of charge traps in the detectors (Knutson et al. 2007; Harrington et al. 2007). This ramp is visible in the top panel of Figure 1, but is weaker than usual for the transit data (the ramp varies due to prior usage of the detector). We removed it by masking out the data near transit, and fitting a parabola to the out-of-transit points. We have considerable experience in fitting to this ramp, via our monitoring of GJ 876 (program 30498). Even strong ramps can be fit by the sum of a linear plus logarithmic function, using linear regression. We applied this more elaborate procedure to the GJ 436

transit ramp, but found no significant difference with the simple parabola fit. In the case of the secondary eclipse (Figure 2), the ramp is stronger, but is still well removed by our full linear + logarithmic fit. We conclude that this ramp is properly reproduced in both cases, and does not contribute significantly to our errors.

3.2. Transit Parameters

A feature of IR transit measurements is the virtual lack of stellar limb darkening. Not only does this produce a simple box-like shape for the transit, but Richardson et al. (2006) suggest that it can increase the radius precision for a given level of photometric precision. Our analysis adopts the (small) limb darkening for GJ 436A based on a Kurucz model atmosphere for 3500/5.0/0.0 in $T_{\text{eff}}/\log(g)/[M/H]$. We verified that changing the stellar temperature, gravity, or metallicity within the errors (Maness et al. 2007; Bean et al. 2006) has negligible effect, because the limb darkening remains small over the plausible range. We integrated the stellar center-to-limb intensities in the Kurucz model over the bandpass of the IRAC 8 μm filter to obtain the limb darkening appropriate to this IR transit. Since this small IR limb darkening is not included in the Claret (2000) prescriptions, we generate theoretical transit curves numerically.

We compute theoretical transit curves by tiling the star in a latitude-longitude grid with zone spacing of 0.18 degrees, and applying the IRAC 8 μm limb darkening. We pass the planet across the numerical star in steps of 0.01 stellar radii, with the planet radius and impact parameter specified in units of the stellar radius. To increase precision, stellar zones at the edge of the planet are adaptively sub-sampled in a 10×10 finer grid. We verified the code’s precision (better than 10^{-6}) by comparing to the Mandel and Agol (2002) analytic non-linear limb darkening cases, and by comparing the depth of synthetic transits to the planet-to-star area ratio (R_p^2/R_*^2), for the case when limb darkening is identically zero.

Fitting to high precision transit photometry requires a determination, or assumption, of the stellar mass (Brown et al. 2001). Gillon et al. (2007a) adopted 0.44 solar masses for GJ 436A, based on the observed luminosity, and they cited the empirical M-dwarf mass-radius relation from Ribas (2006) ($R = M$ in solar units), to justify 0.44 solar radii for the stellar size. Our fit procedure is somewhat different. Given the lack of limb darkening, we can immediately determine the ratio of planet to stellar radius as 0.0839 ± 0.0005 from the depth of the transit (Figure 1). With this value fixed, we generate a grid of transit curves for a range of impact parameters. At each impact parameter, we vary the adopted stellar mass, and compute the transverse velocity of the planet across the star. This computation uses the orbital elements from a fit to the Doppler data (Maness et al. 2007), constrained by the secondary eclipse time (see below). We vary the stellar radius to convert the radius increments on the abscissa of the synthetic transit curve to orbit phase, using the calculated transverse velocity. We include a shift in phase for the synthetic transit curve, to allow for imprecision in the Gillon et al. (2007a) ephemeris. In this manner, we find the best fit stellar radius versus stellar mass, and a revised transit time. We estimate the stellar radius precision from the variation in χ^2 at a given mass.

We intersect the radius versus mass relation ($R \sim M^{0.33}$) from the fitting procedure with the empirical mass-radius relation $R = M$ (Ribas 2006) to find the best stellar mass and radius, and planet radius, at each impact parameter. Repeating this over a grid of impact parameters, we adopt the best fit from the global minimum χ^2 . We determine the error range from $\delta\chi^2$, and from visually inspecting the quality of the fits, paying particular attention to ingress/egress. Our fitting always uses the unbinned data (Figure 1, top), but we bin the data for the lower panel of Figure 1, to better illustrate the quality of the fit. The derived time of transit center is $HJD = 2454280.78149 \pm 0.00016$.

3.3. Secondary Eclipse

The secondary eclipse is shown in Figure 2. The top panel plots the bulk of the data (omitting some points at the outset); the eclipse occurs near the end of the observational sequence, at phase 0.587 ± 0.005 , with amplitude $5.7 \pm 0.8 \times 10^{-4}$ in units of the stellar intensity. Like the transit, all of our fits to this event were made on the original, unbinned data. However, for clarity, the lower panel of Figure 2 shows binned data, expands the phase scale, and overplots the best fit eclipse curve. Our fit constrains the duration of eclipse to equal the duration of transit, finding only the amplitude and central phase.

Table 1 summarizes our results for transit and secondary eclipse.

4. Results and Discussion

Our result for the stellar mass and radius is $M = R = 0.47 \pm 0.02$ in solar units. We are encouraged that these are close to values (0.44) constrained by independent data (Maness et al. 2007). Our derived planet radius is $R_p = 27,600 \pm 1170$ km (4.33 ± 0.18 Earth radii). We conclude that this planet is larger than originally indicated by ground-based photometry (Gillon et al. 2007a). Since this radius is significantly larger than all planets of exclusively solid composition (Seager et al. 2007; Fortney et al. 2007), GJ 436b must have a significant, gaseous, hydrogen-helium envelope. After our transit analysis was complete, we became aware of an independent analysis of the transit data (but not the eclipse data) by Gillon et al. (2007b). These authors do not vary the stellar mass in their fit, but they obtain a very similar radius for this planet, and arrive at essentially the same conclusion.

The observed phase of the secondary eclipse, $\phi = 0.587 \pm 0.005$ indicates that the orbit of GJ 436b is significantly eccentric. Assuming a longitude of pericenter $\varpi = 0$, the magnitude of the observed timing offset indicates a minimum orbital eccentricity,

$$e_{\min} = 0.137 \pm 0.007.$$

Using the constraints provided by the observed times of central transit, $T_c = 2454222.616$ HJD (Gillon et al. 2007a), our $T_c = 2454280.78149$ HJD, and the observed secondary eclipse at $T_s = 2454282.33 \pm 0.01$ HJD, we obtained a set of single-planet Keplerian fits to the radial velocity data published by Maness et al. (2007). A straightforward bootstrap resampling procedure (Press et al. 1992) yields $e = 0.150 \pm 0.012$, $\varpi = 343 \pm 14^\circ$, and $M = 0.070 \pm 0.003 M_{\text{Jup}}$.

As a consequence of its non-zero orbital eccentricity, GJ 436b is likely experiencing asynchronous rotation. Hut (1981) gives an expression for the spin period of a zero-obliquity spin pseudo-synchronized planet:

$$P_{\text{spin}} = \frac{(1 + 3e^2 + \frac{3}{8}e^4)(1 - e^2)^{3/2}}{1 + \frac{15}{2}e^2 + \frac{45}{8}e^4 + \frac{5}{16}e^6} P_{\text{orbit}} \quad (1)$$

For GJ 436b, we find $P_{\text{spin}} = 2.32$ d, which yields a 19-day synodic period for the star as viewed from a fixed longitude on the planet. The large orbital eccentricity also indicates that a significant amount of tidal heating must be occurring. To second order in eccentricity, the tidal luminosity of a spin-synchronous planet (Peale & Cassen 1978; Mardling 2007) is given by:

$$\frac{dE}{dt} = \frac{21}{2} \frac{k_2}{Q} \frac{GM_\star^2 n R_p^5 e^2}{a^6} \quad (2)$$

where k_2 is the planetary potential Love number of degree 2, n is the orbital mean motion, a is the orbital semimajor axis, and Q is the planet’s effective tidal dissipation parameter. The analysis of Levrard et al. (2007) indicates that the tidal luminosity of an asynchronously rotating planet with $e \sim 0.15$ will exceed the value implied by the above expression by a small amount.

If we adopt $T_{\text{eff}} = 3350 K$ for GJ 436A, take a zero albedo for the planet, and assume a uniform re-radiation of heat from the entire planetary surface, we obtain a planetary

$T_{eq} = 642$ K. The somewhat higher temperature ($T = 712 \pm 36$ K) implied by the secondary eclipse depth could arise from inefficient transport of heat to the night side of the planet, from a non-blackbody planetary emission spectrum, from tidal luminosity, or from a combination of the three.

We can estimate Q by assuming $A = 0$, uniform re-radiation, and a blackbody planetary SED to find a fiducial tidal luminosity of 4.7×10^{26} ergssec $^{-1}$, and $\frac{Q}{k_2} = 2.1 \times 10^4$. Assuming $k_2 = 0.34$ (the Jovian value), gives $Q = 7140$. This value is in rough accord with the Q -values measured for Uranus and Neptune. Banfield and Murray (1992) derive $1.2 \times 10^4 < Q_N < 3.3 \times 10^5$ for Neptune, whereas Tittlemore and Wisdom (1989) employ the Uranian satellites to derive $Q_U < 3.9 \times 10^4$. If the planet has maintained $e \sim 0.15$ for billions of years, $Q \sim 7000$ indicates that the planet has radiated tidal energy comparable to the orbital energy and in excess of 100 times its own gravitational binding energy.

Furthermore, $Q \sim 7000$ implies a circularization timescale $\frac{e}{de/dt} \sim 3.0 \times 10^7$ yr. Indeed for any range of Q - which is uncertain even for solar system bodies - the circularization timescale is $< 10^8$ years. It is thus highly likely that an as-yet uncharacterized second planet is providing ongoing gravitational perturbations that allow GJ436b's eccentricity to be maintained over long timescales.

We are grateful to the staff at the Spitzer Science Center for their prompt and efficient scheduling of our observations.

Facilities: Spitzer.

REFERENCES

- Banfield, D., & Murray, N. 1992, *Icarus*, 99, 390.
- Bean, J. L., Benedict, G. F., & Endl, M. 2006, *ApJ* 653, L65.
- Brown, T. M., Charbonneau, D., Gilliland, R. L., Noyes, R. W., & Burrows, A. 2001, *ApJ* 552, 699.
- Butler, R. P., Vogt, S. S., Marcy, G. W., Fischer, D. A., Wright, J. T., Henry, G. W., Laughlin, G. & Lissauer, J. J. 2004, *ApJ* 617, 580.
- Charbonneau, D., Allen, L. E., Megeath, S. T., Torres, G., Alonso, R., Brown, T. M., Gilliland, R. L., Latham, D. W., Mandushev, G., O'Donovan, F., & Sozetti, A. 2005, *ApJ* 626, 523.
- Charbonneau, D., Brown, T. M., Burrows, A., & Laughlin, G. 2007, in *Protostars and Planets V*, eds. D. Jewitt and B. Reipurth, Tucson: Univ. of Arizona Press, p. 701.
- Claret, A. 2000, *A&A* 363, 1081.
- Deming, D., Seager, S., Richardson, L. J., & Harrington, D. 2005, *Nature* 434, 740.
- Deming, D., Harrington, J., Seager, S., & Richardson, L. J. 2006, *ApJ* 644, 560.
- Fazio, G. G., and 64 co-authors. 2004, *ApJ(Suppl)*, 154, 10.
- Fortney, J. J., Marley, M. S., & Barnes, J. W. 2007, *ApJ*, 659, 1661.
- Gillon, M., Pont, F., Demory, B.-O., Mallmann, F., Mayor, M., Mazeh, T., Queloz, D., Shporer, A., Udry, S. & Vuissoz, C. 2007, *A&A Letters*, in press, astro-ph/0705.2219
- Gillon, M., Demory, B.-O., Barman, T., Bonfils, X., Mazeh, T., Udry S., Mayor M., & Queloz, D., 2007, *A&A Letters*, submitted, astro-ph/0707.2261

- Harrington, J., Luszcz, S., Seager, S., Richardson, J. L., & Deming, D. 2007, *Nature* 447, 691.
- Hut, P. 1981, *A&A*, 99, 126.
- Knutson, H. A., Charbonneau, D., Allen, L. E., Fortney, J. J., Agol, E., Cowan, N. B., Showman, A. P., Cooper, C. S. & Megeath, T. 2007, *Nature* 447, 183.
- Levrard, B., Correia, A. C. M., Chabrier, G., Baraffe, I., Selsis, F., & Laskar, J. 2007, *A&A*, 462, L5.
- Mandel, K. & Agol, E. 2002, *ApJ* 580, L171.
- Maness, H. L., Marcy, G. W., Ford, E. B., & Hauschildt, P. H. 2007, *PASP*, 119, 90.
- Mardling, R. A. 2007, *ArXiv e-prints*, 706, arXiv:0706.0224
- Peale, S. J., & Cassen, P. 1978, *Icarus*, 36, 245
- Press, W. H., Teukolsky, S. A., Vetterling, W. T., & Flannery B. P. 1992, *Numerical Recipes*, Cambridge University Press.
- Ribas, I. 2006, *Astr.Sp.Sci.* 304, 89.
- Richardson, L. J., Harrington, J., Seager, S., & Deming, D. 2006, *ApJ*, 649, 1043.
- Seager, S., Kuchner, M., Hier-Majumder, C. A. & Militzer, B. 2007, *ApJ*, in press.
- Tittemore, W. C., & Wisdom, J. 1989, *Icarus*, 78, 63.
- Winn, J. N., Holman, M. J., Henry, G. W., Roussanova, A., Enya, K., Yoshii, Y., Shporer, A., Mazeh, T., Johnson, J. A., Narita, N. & Suto, J. 2004, *ApJ* 617, 580.

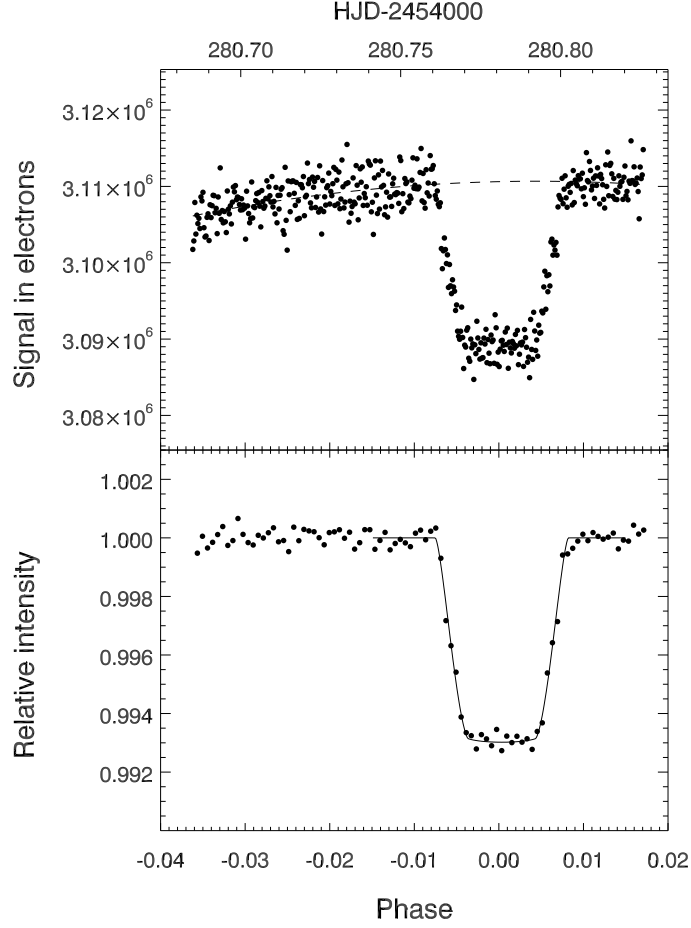


Fig. 1.— Spitzer photometry of the GJ 436b transit with fitted transit curves. Top: photometry before baseline correction. The dashed line is the adopted baseline. Bottom: Baseline-corrected data, binned to approximately 2-minute time resolution (137 sec), with the best fit transit curve. Note the flat bottom that proves a non-grazing transit.

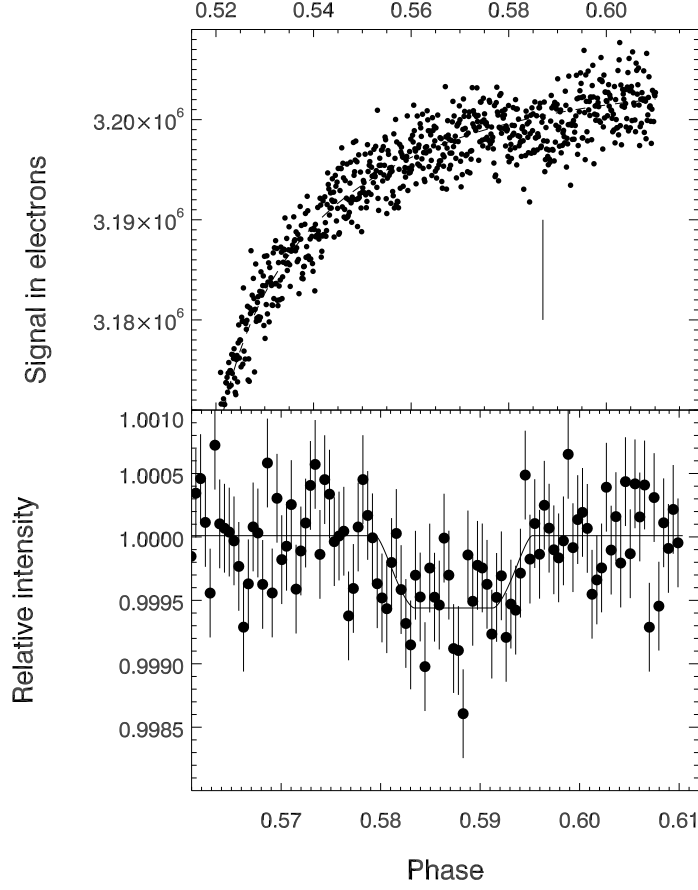


Fig. 2.— Secondary eclipse photometry of GJ 436b. Top: photometry showing the ramp in intensity, with the eclipse marked at phase 0.587. The dashed line is the adopted baseline for points with phase > 0.52 . Bottom: Binned data (102-sec time resolution) shown in comparison to the best fit secondary-eclipse curve, whose amplitude is $5.7 \pm 0.8 \times 10^{-4}$.

Table 1. Derived parameters for GJ 436.

Parameter	Value
Stellar radius ^a	0.47 ± 0.02
Stellar mass	0.47 ± 0.02
Planet radius	$27,600 \pm 1170$ km
Impact parameter	$0.85^{+0.03}_{-0.02}$
Transit time	$HJD = 2454280.78149 \pm 0.00016$
Orbit semi-major axis	0.0291 ± 0.0004 AU
Orbit eccentricity	0.150 ± 0.012
a/R_*	13.2 ± 0.6
Secondary eclipse phase	0.587 ± 0.005
Secondary eclipse amplitude	$5.7 \pm 0.8 \times 10^{-4}$
Planet brightness temperature	712 ± 36 K
Planet mass	$0.070 \pm 0.003 M_{\text{Jup}}$

^aRadius constrained to equal mass, in solar units.